Journal of Power Sources 474 (2020) 228490

Contents lists available at ScienceDirect

Journal of Power Sources

journal homepage: www.elsevier.com/locate/jpowsour

Effect of isotropic and anisotropic porous microstructure on electrochemical performance of Li ion battery cathodes: An experimental and computational study

Milad Azami-Ghadkolai[a], Mehrdad Yousefi[a], Srikanth Allu[c], Stephen Creager[a,b], Rajendra Bordia[a,*]

[a] Department of Materials Science & Engineering, Clemson University, Clemson, SC, 29634, USA
[b] Department of Chemistry, Clemson University, Clemson, SC, 29634, USA
[c] Computational Science and Engineering Division, Oak Ridge National Laboratory, Oak Ridge, TN, 37831, USA

HIGHLIGHTS

- Freeze tape casting creates anisotropically porous battery electrode microstructure.
- 2D finite element analysis performed on anisotropically porosity battery electrode.
- Macroporous channels eliminate Li salt transport limitation in thick electrodes.
- Macroporous channels substantially improve capacity and specific energy.
- Macroporous channels doubles maximum C rates for delivering maximum areal capacity.

GRAPHICAL ABSTRACT

Macroporous channels eliminate Li salt transport limitation of thick electrodes

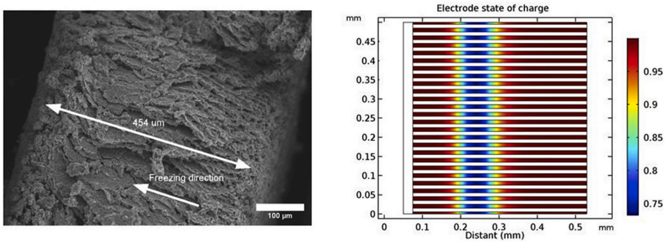

ARTICLE INFO

Keywords:
Thick electrodes
Engineered battery electrode
Li ion battery simulation
Areal capacity optimization

ABSTRACT

Liquid electrolyte mass transport is a major limitation affecting high-power Li ion batteries. Fast discharging causes Li salt depletion in the current collector region of the cathode which produces overpotential in the electrolyte and consequently a drop of cell voltage to below the cut-off voltage, especially at higher electrode thickness and discharge rate. In this study, through experiment and simulation, we have investigated the effect of electrode thickness, mass loading, discharge rate and tortuosity on electrolyte mass transport and final derived areal capacity and specific energy for electrodes having isotropic (normal tape casting) and anisotropic (freeze tape casting) porous microstructure. The macroporous channels in freeze tape cast electrodes facilitate Li salt transport and reduce the Li salt mass transport limitations even at high electrode thickness and discharge rates, and high electrode tortuosity. Computer simulations show that freeze tape cast electrodes may be fully discharged up to 750 μm thickness at 1 C rate compared to 300 μm for normal tape cast electrodes with the same mass loading. Freeze tape cast electrodes also show stable maximum areal capacity for C rates about double the maximum C rates of their normal tape cast electrode counterparts with the same mass loading.

---

* Corresponding author.
E-mail address: rbordia@clemson.edu (R. Bordia).

https://doi.org/10.1016/j.jpowsour.2020.228490
Received 25 December 2019; Received in revised form 20 April 2020; Accepted 10 June 2020

Nomenclature

A	Out of plain area (m^2)
a	Specific interfacial area of the electrode material (m^2)
C_0^e	Initial electrolyte salt concentration (mol m^{-3})
C_s	Lithium concentration in the solid phase (mol m^{-3})
D_s	Lithium diffusion coefficient of solid phase (m^2 s-1)
D_l	Intrinsic electrolyte diffusivity (m^2 s^{-1})
$D_{l,eff}$	Effective electrolyte diffusivity (m^2 s^{-1}) in filling domain
$D_{l,eff,e}$	Effective electrolyte diffusivity in porous electrode (m^2 s^{-1})
$D_{l,eff,sep}$	Effective electrolyte diffusivity in seperator(m^2 s^{-1})
F	Faraday constant (C/mol)
f	Activity coefficient for the salt
I	Total current density (A m^{-2})
i_s	Solid phase current density (A m^{-2})
i_{loc}	Local charge transfer current density(A m^{-2})
i_0	Exchange current density (A m^{-2})
j_n	Pore wall flux
K_l	Intrinsic conductivity of the electrolyte (S m^{-1})
$K_{l,eff}$	Effective conductivity of the electrolyte in filling domain (S m^{-1})
$K_{l,eff,e}$	Effective conductivity of the electrolyte in porous electrode (S m^{-1})
$K_{l,eff,sep}$	Effective conductivity of the electrolyte in porous electrode (S m^{-1})
L	Electrode thickness (m)
L	sep Separator thickness (m)
L_d	Electrolyte penetration depth (m)
n	Number of wall
OCV	Open circuit potential (V)
Q_V	Volumetric capacity mAh cm^{-3})
Q_A	Areal capacity (mAh cm^{-2})
Rp	Active material particle size (m)
Rho	Density (gr/cm^3)
SOC	Sate of charge
T	Temperature (K)
t	Time(s)
t_+	Transport number of the electrolyte
W_total	Total width (m)
W_lto	Cathode width (m)
W_elec	Electrolyte width (m)
α	Anodic/cathodic charge transfer coefficient
ΔE_s	Potential difference between consecutive relaxations (V)
ΔE_t	Potential difference incurred due to applied current (V)
ϵ_s	Volume fraction of active material in each cathode wall
ϵ_ω	Porosity of each porous electrode wall
ϵ_{ina}	Volume fraction of inactive components in each Cathode wall
ϵ_l	Volume fraction of electrolyte in filling domain
$\epsilon_{l,e}$	Volume fraction of electrolyte in porosity of porous electrode
ϵ_{sep}	Porosity of separator (or volume fraction electrolyte into porosity of separator)
η	Overpotential (V)
κ	Electrolyte conductivity (S/m)
σ_s	Electrical conductivity (S m^{-1})
τ	Tortuosity
$\varnothing_l$	Electrolyte potential (V)
$\varnothing_s$	Electric potential (V)
ϑ	Reaction rate ($m^{2.5}$ $(mol^{0.5}.s)^{-1}$)
$+$	An epsilon more positive
$-$	An epsilon more negative

1. Introduction and background

Increased energy and power density are highly sought in electrochemical energy storage cells. To increase the energy and power density, discovery of new materials with high theoretical capacity and excellent transport properties is of great importance. An alternative way of improving energy and power density using existing materials is increasing the mass loading and therefore the thickness of electrodes. Thick electrodes are highly desired because they have high mass fraction of active material, and therefore high specific capacity. Maximizing power density in thick electrodes necessitates adoption of an intricate electrode architecture that typically consists of three intertwined phases. Each phase has a different functionality. Active material serves to store the charge via redox reactions, electronically-conductive materials such as carbon black assist in transfer of electrons to/from active material, and the ionically-conductive phase assists in transfer of ions to/from active material. The ionically-conductive phase is typically the pore spaces of the electrode which are filled with liquid electrolyte. With the discovery of high-energy-density but low-conductivity active materials like $LiFePO_4$ (LFP) and $Li_4Ti_5O_{12}$ (LTO), the need for advanced techniques for introducing fine multimodal features into electrode microstructure while preserving the interconnectivity of all the three phases is more pressing than ever. An additional advantage of this approach is that, with suitable microstructure design, it can be adopted for new materials as they are developed.

Highly tortuous electrode microstructures produced using conventional fabrication methods cause portions of active material to have low accessibility to liquid electrolyte especially at high thickness [1], reducing both power and energy density. Electrode microstructures designed to have fast ion and electron transport pathways are needed. Electrodes having spatially ordered and interconnected macroporous structures [2,3], and hierarchical pore size distributions [4–9] show improved energy and power density compared with electrodes lacking such features. Interconnected macropores can be created in electrodes by templating [10–13], freeze casting [14–17], stamping [18] and nano casting [4], and by using sol-gel methods [6]. Several reports describe thick macroporous electrodes that show rapid charging. Sebastian Behr and co-workers used freeze casting followed by a sintering technique to produce highly structured additive-free Li ion nickel cobalt aluminum oxide (NCA) electrodes [14]. Ruhul Amin and co-workers prepared high energy density graphite electrode [19] through freeze casting and Benjamin Delattre and co-workers [20] reported three to fourfold increase of area specific energy density through freeze casting of NCA.

This paper focusses specifically on comparing electrodes with and without the macroscopic pores, for similar area-normalized loadings. It includes comparison of experiment with computational modeling, and uses modeling to make predictions about behavior under conditions different from those used for experiments. We employ freeze tape casting, a combination of freeze casting and tape casting, to introduce hierarchical multimodal interconnected unidirectional macropores into the electrode structure [15]. This approach enabled the synthesis of thick electrodes that retain higher capacity at faster charging rates compared to normal tape cast electrodes. An additional advantage of this method is that it eliminates the secondary step of sintering and also cutting which makes it suitable for manufacturing.

Classical models of battery electrode behavior such as that due to Newman have been used since 1993 [21,22] and are good for predicting behavior in relatively simple electrodes where continuum assumptions are appropriate. Macroporous electrodes require extension of these models to include the possibility of multiple interconnected domains having different properties. We report here on use of Multiphysics methods in COMSOL for simulating the behavior of normal tape cast as well as freeze tape cast porous electrodes. We treat the freeze tape cast electrode as a series of slab-shaped electrolyte pores that are interspersed between slabs of active electrolyte material. The model is schematically illustrated in Fig. 1.

In addition to the effect of microstructure design, the effect of electrode material tortuosity is also investigated. A wide range of tortuosity values is reported in literature for lithium battery electrode materials. Doyle and co-workers reported a tortuosity value of 2.9 for a $LiMn_2O_4$ electrode [23] and Stephenson reported values of 21–27 for a $LiCoO_2$ [24] electrode. Apart from porosity which has a strong effect on tortuosity, there are many other parameters that can have a direct effect on battery electrode tortuosity. Particle shape, conductive agent size and morphology, electrode composition, and binder layer thickness around the active material are among the most influential factors affecting electrode tortuosity. Landesfeind and coworkers [25] showed that with increasing amount and layer thickness of binder, tortuosity increases sharply from 3.8 to 5.5 by increasing binder layer thickness from 2 to 10 nm in the absence of Timcal Carbon C65. Addition of C65 carbon causes tortuosity to decrease, probably due to the high surface area and porosity of C65. Landesfeind and co-workers [25] also showed that the binder composition has a prominent effect on tortuosity. For a binder layer thickness range of 5–17 nm, a Kureha-type binder shows a tortuosity range of 3–4.2 whereas a CMC/SBR-type binder shows a tortuosity of 5–10. Due to this strong dependency of tortuosity on binder material, in this study, we use simulation methods to study the effect of tortuosity by investigating tortuosity up to 10 as an upper limit for electrode materials.

Spinel $Li_4Ti_5O_{12}$ (LTO) as one promising alternative to graphite for lithium battery anodes is the subject of this study. Very high rate capability, outstanding cycle ability due to low volume change in the lithium insertion/extraction process [26], and minimum SEI formation [27–29] make LTO a useful electrode material for batteries. In this paper, molybdenum-doped LTO ($Li_4Ti_{4.7}Mo_{0.3}O_{12}$, MoLTO) was synthesized through a simple solid state method as described in our previous work [15,30]. Particle size distribution of the powder measured by a LS 13 320 Laser Diffraction Particle Size Analyser (Beckman Coulter) is shown in Figure S 7 in the supporting information. We note that LTO and MoLTO are of interest as lithium battery anodes but in this research, they were studied as cathodes, against a Li metal anode. Reactions described here as cell discharge reactions would thus be cell charging reactions when the LTO or MoLTO electrode is used as anode together with a conventional cathode material, e.g. $LiFePO_4$ or $LiCoO_2$.

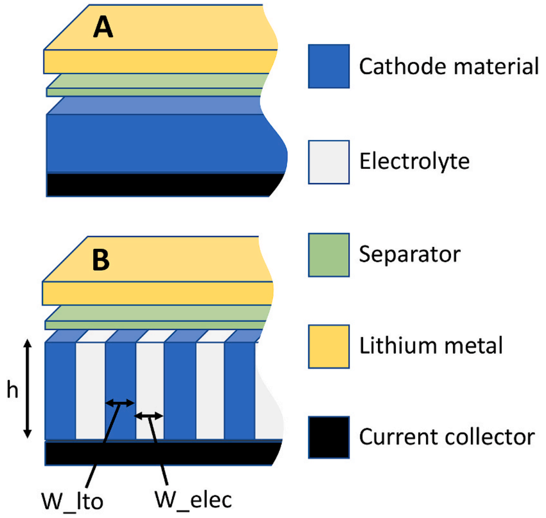

Fig. 1. Simulation geometry for (A) normal tape-cast electrodes; and (B) freeze tape cast electrodes. Anode and cathode are both in intimate contact with separator; gaps are shown only for clarity. Separator is filled with electrolyte.

2. Experimental and computational methods

2.1. Electrode and cell fabrication

All electrodes studied in this work were fabricated from molybdenum-doped lithium titanate (MoLTO) that was prepared as previously described [15]. Tape-cast electrodes were made from a slurry containing active materials powder (MoLTO, 85.93 wt%), Timcal graphite powder (9.57 wt%, MTI Corporation), carboxymethyl cellulose (CMC, 0.8 wt%, MTI corporation) and styrene-butadiene rubber (SBR, 3.7 wt%, MTI corporation) in distilled water. The wt% solids in the slurry is 50.86%. Once the slurry is ready, it is poured over a piece of battery-grade copper foil (MTI corporation-11 μm thick coated with conductive carbon) using a dispenser followed by tape casting using the doctor blade adjusted to the desired liquid film thickness. Normal tape-cast samples were then dried in ambient atmosphere. In the case of freeze tape casting, after the slurry is spread on the current collector, without any delay the tape is placed over a cold copper finger (already set at the desired temperature) to freeze the slurry. Frozen tapes were then immediately freeze dried at temperature of −20 °C and pressure 0.03 mbar for 3 h to remove the ice and leave behind hierarchical anisotropic porous electrodes. After punching, samples were vacuum dried for 24 h at 80 C. Charge-discharge experiments were done on disk-shaped half-cell MoLTO electrodes with 0.7084 cm^2 area, using Li metal disk as the opposite electrode. Cells were assembled in an MTI split cell with a MoLTO electrode and a lithium metal electrode separated by a porous polymer separator (Celgard 2325, 25 μm microporous trilayer PP/PE/PP membrane). A 1 M $LiPF_6$, 3:7 EC: EMC electrolyte solution was used to form all Li ion battery cells. Cell assembly was performed in an argon-filled glove box. Galvanostatic charge-discharge testing was performed over a cell potential range from 1.0 to 2.5 V using a battery analyzer (BST8-WA, MTI). Charging of the half-cell was performed in a constant current/constant voltage mode (CC/CV) with rate of C/5 for all the conditions.

2.2. Electrode geometry and properties

An electrode that was tape cast with a 454 μm wet thickness, corresponding to a mass loading of 30.2 mg cm^{-2}, was found experimentally to produce electrodes of thickness 250 μm for normal tape casting and 454 μm for freeze tape casting. Calculated values for simulations for electrodes having different mass loadings and thicknesses are obtained by assuming proportionality in thickness and mass loading.

The porous normal tape cast electrode material consists of 35% MoLTO, 13% filler (a combination of CMC, SBR binders and carbon), and 52% porosity by volume which were calculated based on the density and weight percent of all the components, and the measured thickness of the tape. The porous freeze tape cast electrode material consists of 19% MoLTO, 7% filler (a combination of CMC, SBR binders and carbon), and 73% porosity by volume.

The structure, morphology and thickness of the synthesized electrodes were characterized by scanning electron microscopy (FESEM, S-4800 Hitachi). SEM micrographs of normal and freeze tape cast samples with thickness of 250 and 454 μm respectively (mass loading 30.22 mg cm^{-2}) are shown in Figure S 6 in the supporting information.

The geometric parameters needed for the simulation of the normal and freeze tape cast are shown in Table 1.

The freeze tape cast electrode geometry is constructed by varying the height *h* representing the thickness of the electrode. Each wall of porous cathode active material has thickness *W_lto* and height *h*. In between each wall of porous cathode active material there is a region of

Table 1
Geometric parameters for electrode design.

Parameters	Units	Descriptions	Normal electrode	Freeze tape cast electrode
h	mm	Thickness	Varied[a]	Varied[a]
W_lto	mm	Cathode width	0.5	0.01
W_elec	mm	Electrolyte width	0	0.01
n		Number of cathode walls	1	25
W_tot	mm	Total width	0.5	0.5
A	mm^2	Out of plane area	70.84	70.84
$\boldsymbol{\epsilon_s}$		Volume fraction of active material in each cathode wall	0.3538	0.3891
$\boldsymbol{\epsilon_w}$		Porosity of each cathode wall	0.5162	0.4678
$\boldsymbol{\epsilon_{ina}}$		Volume fraction of inactive components in each Cathode wall	0.13	0.1431

[a] The mass loading at different thicknesses is proportional to the thickness. Based on the experimental result for 250 μm normal and 454 μm freeze tape cast is 30.22 mg cm^{-2}.

electrolyte with width of *W_elec* and same height of *h*. By recalculation of volume percent of each component in freeze tape cast sample cathode wall knowing that total porosity is 73.3% and 50% is macroporosity, new values of 38.91% MoLTO, 14.31% filler, and 46.78% microporosity by volume can be obtained for each cathode's walls. For simulation of thicker and thinner electrodes, we kept, *A*, out of plane area fixed and only changed the *h* in a way to meet target mass loading. Table 1 shows all the geometrical parameters used in defining the model geometry.

2.3. Computational modeling

All computational modeling work was performed using the lithium battery module in COMSOL. The following narrative summarizes the relevant physical models.

In the solid phase for the lithium insertion material, mass balance in the electrode is governed by Fick's second law of diffusion [21,22,31–35].

$$\frac{\partial C_s}{\partial t} = -\nabla.(-D_s.\nabla C_s) \qquad \text{Eq 1}$$

$$\frac{\partial C_s}{\partial r} = 0 \ at \ r = 0 \qquad \text{Eq 2}$$

In these equations C_s is lithium concentration in the solid phase and D_s is Li diffusivity in the solid. No flux condition is applied at the center of particle due to symmetry and pore wall flux $(j_n = i_{loc}/F)$.

In the solid phase, the current density is defined as a function of the effective electrical conductivity, $\sigma_{s,eff}$, and the gradient of the electric potential, $\varnothing_s$, by Ohm's law.

$$i_s = -\sigma_{s,eff}\nabla\varnothing_s \qquad \text{Eq 3}$$

$$\sigma_{s,eff} = \sigma_s {\varepsilon_s}^{1.5} \qquad \text{Eq 4}$$

$$\frac{\partial\varnothing_s}{\partial x} = -\frac{I}{\sigma_{s,\ eff}} \ at \ x = l \ (current \ collecter) \qquad \text{Eq 5}$$

$$\frac{\partial\varnothing_s}{\partial x} = 0 \ at \ x = 0 \ (seperator - electrode \ surface) \qquad \text{Eq 6}$$

In these equations, ϵ_s is volume fraction of solid and *I* is total current applied. Equations (5) and (6) are solid phase potential boundary conditions at current collector and separator-current collector surfaces.

For the transport of lithium ion inside the electrolyte the concentrated solution theory is used, which can be written as Eq (7). Effective electrolyte diffusivity can be also calculated using Equation (8) through definition of tortuosity which was measured as shown in supporting material. See Sections 2.4 and 2.5 and Figs. S4 and S5 in the supporting material for details.

$$\varepsilon_l\frac{\partial C_l}{\partial t} = \nabla.\left(D_{l,eff}\nabla C_l\right) + \left(\frac{ai_{loc}}{F}\right)(1-t_+) \qquad \text{Eq 7}$$

$$D_{l,eff} = D_l\frac{\varepsilon_l}{\tau} \qquad \text{Eq 8}$$

$$\frac{\partial C_l}{\partial x} = 0 \ at \ x = l \ (current \ collecter) \qquad \text{Eq 9}$$

$$C_{x-} = C_{x+} \ at \ \ x = 0 \ (\ seperator - electrode \ surface) \qquad \text{Eq 10}$$

$$D_{l,eff,sep}\frac{\partial C_l}{\partial x^-} = D_{l,eff,e}\frac{\partial C_l}{\partial x^+} \ at \ x = 0 \ (separator - electrode \ surface) \qquad \text{Eq 11}$$

In these equations ε_l is a volume fraction of electrolyte (or porosity) in the region for liquid electrolyte filling, including the separator and porous electrode. It is equal to the microporosity within the walls in the freeze tape casting electrodes and its value is 1 in the electrolyte pillars representative of unidirectional macropores. C_l in equation (5) denotes electrolyte salt concentration. D_l , $D_{l,eff}$ and $D_{l,eff,sep}$denote electrolyte intrinsic Li ion diffusivity, effective Li ion diffusivity in porous electrode and effective Li ion diffusivity in porous separator, respectively. i_{loc} denotes local charge transfer current density. Equations (9)–(11) show boundary conditions of electrolyte transport and concentration on current collector and separator-electrode surfaces.

$$-D_s\frac{\partial C_s}{\partial r} = j_n at \ r = r_p \qquad \text{Eq 12}$$

$$aj_n = \frac{ai_{loc}}{F} = \frac{\nabla.i_l}{F} \qquad \text{Eq 13}$$

In equations (12) and (13) j_n is the pore wall flux (it can be also used as a boundary condition at the particle surface), *a* is the specific interfacial area of the electrode material and can be calculated by $a = \frac{3\varepsilon_s}{r}$ where $\varepsilon_s$is volume fraction of active material and *r* is active material particle radius.

Electrolyte current is governed by an extended version of Ohm's law through Equation (14). Equations (16)–(20) shows boundary conditions on electrolyte conductivity and potentials at current collector, Li metal-separator and separator-electrode surfaces.

$$i_l = -K_{l,eff}\nabla\varnothing_l + \left(\frac{2K_{l,eff}RT}{F}\right)\left(1+\frac{\partial lnf}{\partial lnC_l}\right)(1-t_+)\nabla lnC_l \qquad \text{Eq 14}$$

$$K_{l,eff} = K_l\frac{\varepsilon_l}{\tau} \qquad \text{Eq 15}$$

$$K_{l,eff,sep}\frac{\partial\varnothing_l}{\partial x^-} = K_{l,eff,e}\frac{\partial\varnothing_l}{\partial x^+} \ at \ x = 0 \ (separator - electrode \ surface) \qquad \text{Eq 16}$$

$$\frac{\partial \ \varnothing_l}{\partial x} = 0 \ at \ x = l \ (current \ collecter) \qquad \text{Eq 17}$$

$$\varnothing_l = 0 \ at \ x = l \ (current \ collecter) \qquad \text{Eq 18}$$

$$\varnothing_l = 0 \ at \ x = -l_{sep} \ (Li \ metal - separator \ surface) \qquad \text{Eq 19}$$

$$\varnothing_{l,x^+} = \varnothing_{l,x^-} \ at \ x = 0 \ (separator - electrode \ surface) \qquad \text{Eq 20}$$

In these equations K_l, is the intrinsic ionic conductivity of electrolyte. $K_{l,eff}$, $K_{l,eff,e}$ *and* $K_{l,eff,sep}$ are effective ionic conductivity of electrolyte in filling domain, electrolyte in porous electrode, and electrolyte in separator, respectively. $\varnothing_l$ is the electrolyte potential, *f* is the activity coefficient for the salt, and t_+ is the lithium cation transport number of the electrolyte. Equation (15) denotes the effective electrolyte conductivity in filling domain using tortuosity τ of that domain (either porous separator or electrode). These tortuosities have been obtained experimentally as described in the supporting material, specifically in Section 2.4 and 2.5 respectively for separator and electrode.

Charge transfer reaction between the electrolyte phase and active material is described by the Butler-Volmer equation (21))

$$i_{loc} = i_0 \left[\exp\left(\frac{\alpha F}{RT} \eta \right) - \exp\left(- \frac{(1-\alpha)F}{RT} \eta \right) \right] \qquad \text{Eq 21}$$

$$i_0 = F(\vartheta_c)^{\alpha}(\vartheta_a)^{\alpha}(C_{s,max} - C_s)^{\alpha}(C_s)^{\alpha}(C_l)^{\alpha} \qquad \text{Eq 22}$$

In this equation i_0 is exchange current density, α is anodic/cathodic charge transfer coefficient, ϑ_a and ϑ_c denote the anodic and cathodic reaction rates, respectively. $c_{s,max}$ - c_s represents the concentration of empty sites at the surface of the cathode particles, while c_l represents the salt concentration. For Li metal side, equation (21) was used with the exchange current density of Li metal obtained experimentally as detailed in Section 2.3 of the supporting material. η is overpotential which is defined by

$$\eta = \varnothing_s - \varnothing_l - OCV \qquad \text{Eq 23}$$

In this equation, OCV is the open circuit potential of active material.

A 1 M $LiPF_6$ in EC: EMC (3:7) weight ratio electrolyte is used in the model. Ionic conductivity, diffusion coefficient, lithium-ion transport number, and activity are the most important transport properties which need to be determined as a function of salt concentration. Andreas Nyman and coworkers [36] obtained ionic conductivity (mS/cm) as function of salt concentration $C_l(M)$ for 0–2.2 M, Li diffusion coefficient (m^2/s) data for $C_l(M)$ of 0–2 M, transport number and activity data for $C_l(M)$ of 0.2–2 M at temperature of 298 K. These data are in the supporting material (Section 1) and were used as a reference in this study. Transport properties outside of this concentration range were taken as constant, independent of concentration, rather than linear because a linear extrapolation predicts negative conductivity for very high salt concentrations, which is a non-physical result leading to simulations that do not converge.

2.4. *Material properties*

Further details on measurement of material properties—including separator tortuosity, electrode tortuosity, active material OCV and Li ion diffusion coefficient as a function of SOC, and Li metal exchange curent density—are presented in the supporting material (Section 2). Material parameters used in the simulations are shown in Table 2.

A structured grid mesh with elements sized to 1 μm with an aspect ratio of 1 was used in all the simulations. The MUMPS (Multifrontal Massively Parallel) direct solver was used in COMSOL 5.3a with maximum time steps limited to 10 s increments with a tolerance factor of 10^{-3}. All models were distributed across 24 dual Intel Xeon 6148G scalable processors Dell R740 core Linux cluster nodes of Palmetto cluster of Clemson university with 128 GB of RAM each with a run time around 5–7 h for each case depending on the size of the model.

3. Results and discussion

Fig. 2 shows simulated and measured discharge curves for normal and freeze tape cast electrodes having thicknesses of 250 and 454 μm respectively and a mass loading of 30.22 mg cm^{-2}, at different discharge rates. Both experiment and simulation show a limiting specific capacity of just under 5 mAh g^{-1} at low C-rate, with some loss of capacity at the cutoff voltage of 1.0 V at rates above 1 C. At the lower discharge rates of 0.2 and 0.5 C the simulations match very well with experiment, however, at the higher discharge rates the experimental results and the simulation start to deviate slightly from each other.

It should be noted that experimental results on a thinner electrode of thicknesses 150 μm for a normal tape cast were also collected and there was excellent match at all the C rates of 0.5–2C, shown in supporting material Section 3 and Figure S 8. We have chosen to show the experimental result of 250 of normal and 454 of freeze cast to substantiate the point that at high thicknesses and high C rates other important parameters such as particle size and shape distribution, inhomogeneity through the thickness of electrode, parasitic reactions, and the difference between real 3D microstructure with the idealized 2D microstructure causes higher overpotential of experiments compared to idealized simulations. To the best of our knowledge, the quite good agreement between experiment and simulation at high electrode thicknesses of 150 and 250 μm has not been reported, which indicates that the parameters chosen for the computational model are appropriate. Mohammad Rashid and co-workers [37] have recently reported a good match of experiment and simulation on LTO with the electrode thickness as thin as 15 μm. Also, Ali Ghorbani Kashkoli and co-workers [35] reported deviation of experiment from simulation at C rates of 1 and 5 for LTO electrode thickness of 20 μm.

Table 2
Materials parameters used in simulations.

Material parameters used in simulation	Definition	Value	unit	ref
$\mathbf{D_{Li}}$	Lithium diffusion coefficient	1×10^{-17}	$m^2\ s^{-1}$	Measured [Supp]
Rp	Particle size radius	100	nm	Measured [Supp]
$\boldsymbol{\sigma}$	MoLTO electronic conductivity	1	$S\ m^{-1}$	Measured [Supp]
$\mathbf{c_0^e}$	Initial electrolyte salt concentration	1000	$mol\ m^{-3}$	Sigma alderich
$\mathbf{SOC_{min}}$	Minimum state of charge	0.003	–	Measured [Supp]
$\mathbf{SOC_{max}}$	Maximum state of charge	0.9	–	Measured [Supp]
$\boldsymbol{\alpha_a, \alpha_c}$	Anodic/cathodic charge transfer coefficient	0.5	–	Assumed
$\boldsymbol{\tau}$	Tortuosity[a]	5	–	Measured [Supp]
ϑ	Rate constant of active material	5×10^{-11}	$m^{2.5}\ (mol^{0.5}.s)^{-1}$	[37]
rho	Density of active material	3.43	$g\ cm^{-3}$	

[a] Tortuosity of normal tape cast electrode measured and assumed to be same within the walls of freeze tape cast electrodes. Tortuosity of separator is measured to be 4.02.

It should be noted that both experiments and simulations show that the FTC electrodes lead to higher capacity compared to that for NTC especially at higher discharge rate. In addition, FTC shows higher overpotential in the earlier discharge range. This is because the FTC experiences higher ohmic loss (resistance) because of its higher current density due to its higher thickness and higher porosity. This effect is most pronounced at the early stage of discharge because of high electrolyte concentration which results in minimal electrolyte overpotential.

After the validation of the simulations by the comparison of the simulated and measured discharge curves (Fig. 2), a series of simulations was conducted at variable mass loading, electrode thickness and discharge rates for both normal and freeze tape cast electrodes. The results of these simulations are presented in Fig. 3 as plots of areal discharge capacity vs electrode thickness (Fig. 3a) and mass loading (Fig. 3b). For the thinner electrodes (i.e., $<$ 150 μm) having the lower mass loadings ($<$20 mg cm^{-2}), the simulated discharge capacity is proportional to the electrode thickness and mass loading at all discharge rates for both normal and freeze tape cast electrodes. This behavior indicates that the full electrode capacity is accessed. After passing a critical thickness or mass loading at each C rate, further increase in thickness or mass loading does not result in proportionally more capacity. This behavior indicates that some of the available capacity is not being accessed. Finally, after passing a thickness or mass loading having

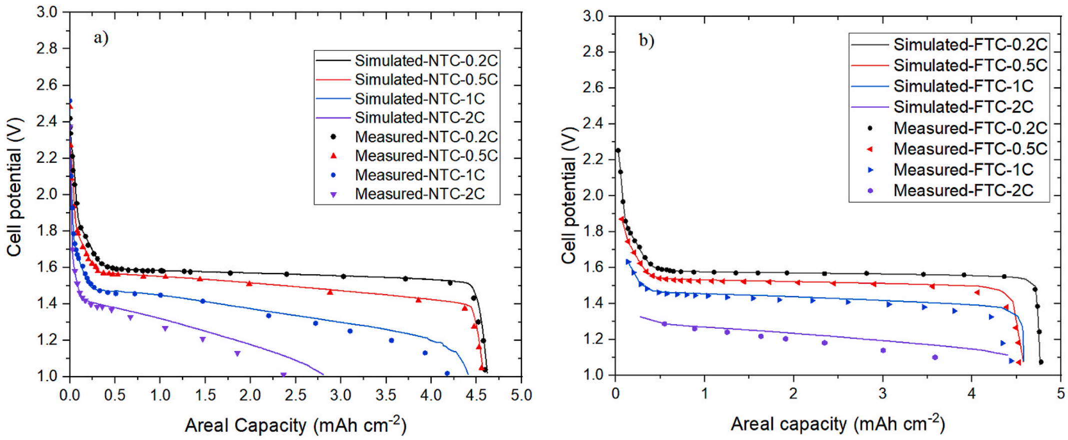

Fig. 2. Simulated and measured discharge curves for a) normal tape cast electrode with thickness of 250 μm and b) freeze tape cast electrode with thickness of 454 μm with same mass loading of 30.22. Discharge curves were measured and simulated at C rate of 0.2, 0.5, 1 and 2C.

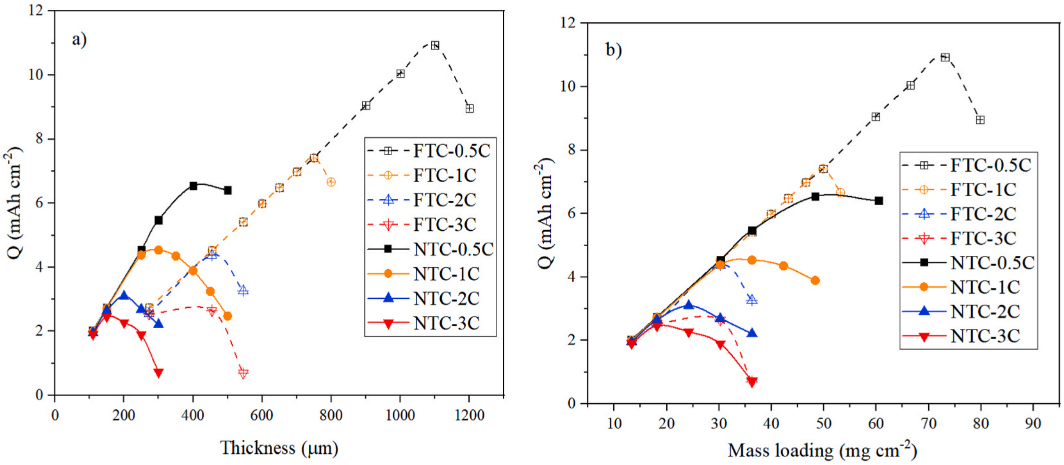

Fig. 3. Areal capacity of normal and freeze tape cast electrode at different C rates as a function of a) thickness b) mass loading.

a maximum capacity, higher thickness or mass loading results in lower areal capacity. Clearly, the higher mass-loading electrodes have large portions of active material that are inaccessible at the rates investigated in this work (0.5–3 C).

It is interesting to compare the results for freeze and normal tape cast electrodes. The simulations in Fig. 3a show that freeze cast electrodes may be fully discharged up to 750 μm thickness at 1 C rate, 454 μm thickness at 2 C rate and 300 μm thickness at 3 C rate. In contrast, normal tape cast electrodes achieve maximum areal capacity at thickness of 350, 200 and 150 μm at the same discharge rates. Fig. 3b shows a similar effect but with the data plotted as a function of mass loading. Both plots show that electrodes having the macroporous freeze cast architecture provide access to a larger capacity than those having the normal tape cast architecture, for the same discharge rate and mass loading. It seems likely that the beneficial effects of the macroporous freeze-cast architecture have to do with improved electrolyte transport.

In order to more fully appreciate the effect of electrode microstructure on electrolyte transport and discharging, Li salt concentration as well as active material local state of charge (SOC) for normal and freeze tape cast electrodes as a function of discharge time and spatial position in the electrodes were investigated and are depicted in Figs. 4 and 5. Fig. 4 considers the case of a normal tape cast electrode that is 250 μm thick with a mass loading of 30.22 mg cm^{-2}, for discharge rates of 0.5 C, 1 C and 2C. In Fig. 4, a distance of 0 corresponds to the location where the electrode is in contact with the separator, and distance of 250 μm corresponds to the location where the electrode is in contact with the current collector. In the narrative below we consider the results for the cases of low rate discharging, high rate discharging, and intermediate rate discharging.

Low-rate discharge. The plots for discharge at 0.5 C (Fig. 4 a and b) show that electrolyte concentration initially decreases near the current collector and increases near the separator, and the electrode state of charge initially rises uniformly near the current collector but to a greater extent near the separator. This finding is rationalized as follows. As the electrode discharges, lithium salt is consumed in the electrode pore spaces and is replenished by transport from the separator side of the electrode. Salt concentration thus falls everywhere in the electrode but also rises in the regions nearest to the separator. This situation creates a salt concentration profile within the electrode, with salt concentration highest near the separator and lowest near the current collector. A high local salt concentration in the electrode pore spaces nearest to the separator has the effect of causing those parts of the electrode nearest to the separator to discharge preferentially compared to those parts of the electrode nearer to the current collector. This phenomenon is readily seen in Fig. 4b thru plots of state of charge vs position in the electrode for various times following the start of discharge. For example, after 1000 s the electrode is discharged uniformly and to a small extent in the regions nearest to current collector but to a much greater extent in the region nearest to the separator. This finding is rationalized as follows. A high local salt concentration causes the local electrolyte concentration overpotential to decrease, which causes the regions where salt concentration is highest to experience a greater driving force for electrode

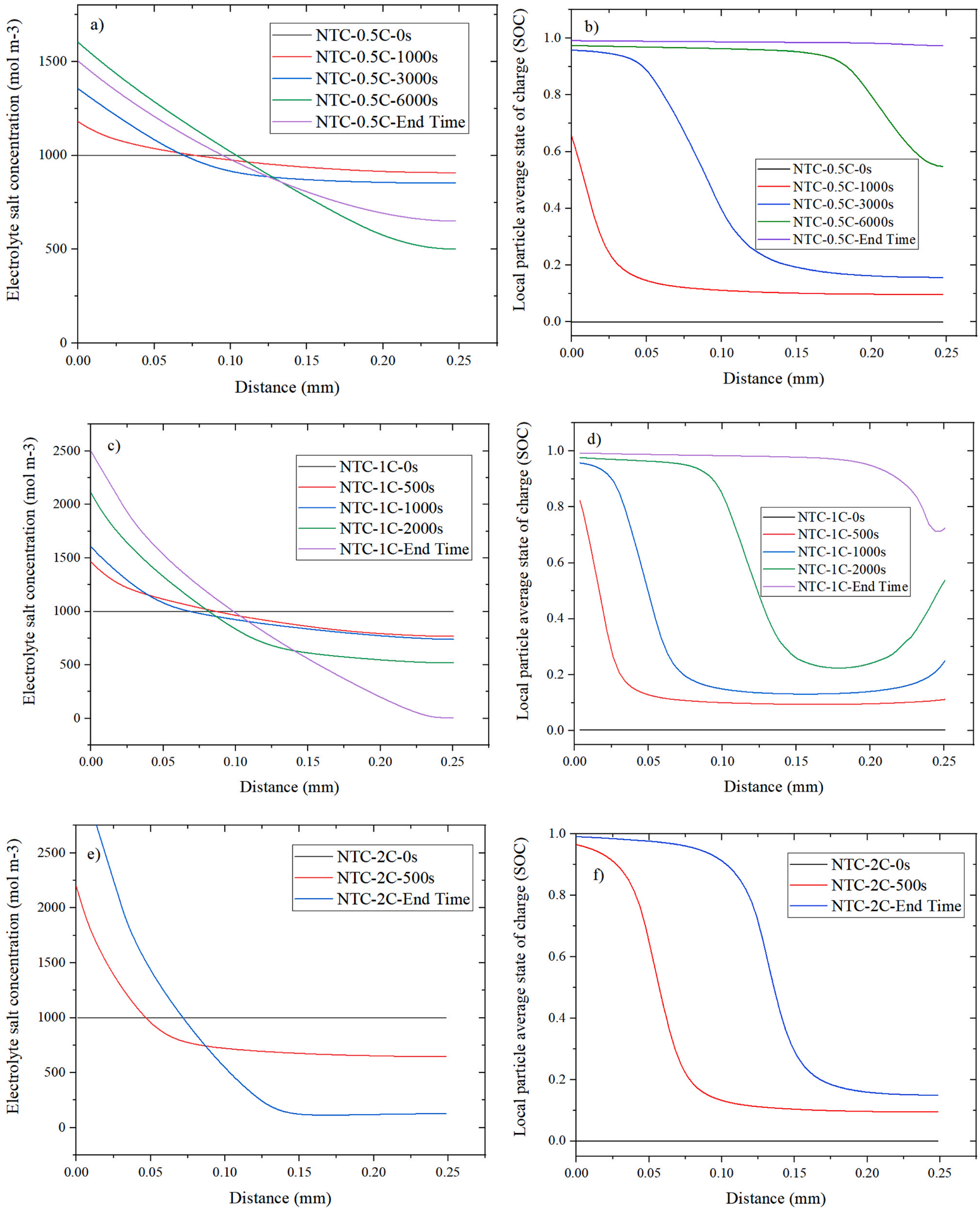

Fig. 4. a,b) Electrolyte concentration and Local SOC as a function of electrode thickness for normal tape cast electrode with thickness of 250 μm at a,b) 0.5, c,d) 1 and e,f) 2 C. Note: Distant 0 is separator-electrode surface, distant 0.25 mm is current collector side and end time means the end of discharge time which for 0.5, 1 and 2C are 6650s, 3206s and 1023s, respectively.

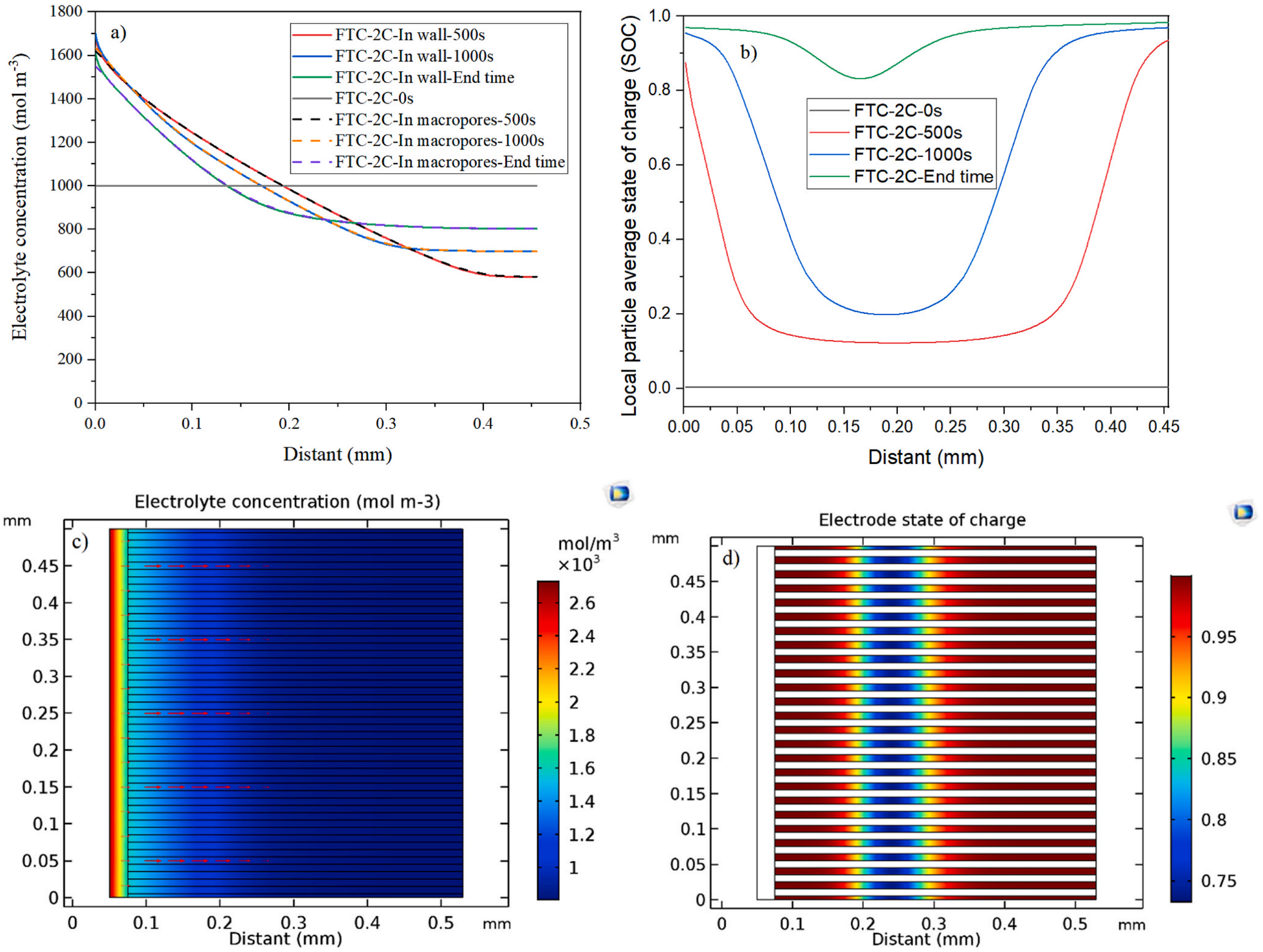

Fig. 5. a) Electrolyte concentration in in the middle of wall and macropores b) local state of charge (SOC) in the middle of wall c) 2D graph of electrolyte concentration at the end of discharge d) 2D graph of SOC at the end of discharge through thickness of the electrode with 454.5 μm thickness discharging at 2C.

discharge. The potential difference caused by differences in the concentration of Li ion (charge-carriers) between locally close regions in electrolyte is called local electrolyte concentration overpotential.

The net effect is to cause the electrode to discharge from the outside in, with the last parts to discharge being those nearest to the current collector. This latter point is evident in the two curves at longest times in Fig. 4b, which show the electrode to be fully discharged in the regions nearest the separator but with some small amount of remaining capacity left to discharge in the regions near the current collector. At the end of discharge, the local SOC has changed from 0 to 1 for nearly the entire electrode, consistent with the fact that, at this slow discharge rate, the full available capacity may be accessed.

High-rate discharge. Fig. 4 e and f show variations in salt concentration and local state of charge during discharge for the same electrode when using a much higher discharge rate of 2C. The initial trends are similar to those seen at low discharge rate, except that they occur more rapidly. After 500 s a salt concentration polarization gradient has developed with salt concentration diminished uniformly in regions near the current collector and significantly elevated in regions near the separator. The effects on local state of charge (Fig. 4f) are similar to those in Fig. 4b; the region near the current collector is uniformly discharged to a small degree and the region near the separator is discharged to a much higher degree, such that the electrode is again discharging from the outside in. A significant difference for the higher discharge rate is that the discharge ends shortly after 500 s. At this time the salt concentration in the electrode pore spaces in regions near the current collector has dropped to nearly zero. This situation causes the electrolyte concentration overpotential near the current collector to become very large, such that a large applied potential is needed to drive the electrode reaction. The cell potential drops below the designated cutoff value of 1 V, thereby stopping the discharge. At the time the discharge is stopped, the electrode regions near the separator are almost fully discharged but the regions near the current collector are much less charged, such that the overall discharge capacity ends up being a small fraction of the total available capacity. These finding illustrate the role that salt transport, and especially local salt concentration, plays in determining the capacity available from discharge at a particular rate.

Intermediate-rate discharge. Fig. 4 c and d illustrate the changes in salt concentration and local SOC during discharge at an intermediate rate of 1C. At short times of 500 and 1000 s the trends are the same as for low-rate discharge, i.e. a salt concentration polarization develops with high salt concentration near the separator, and electrode discharge occurs uniformly near the current collector and also preferentially near the separator. After 2000 s an unusual effect is seen whereby a high extent of discharge is seen in the regions near the separator and also near the current collector. It is as if the electrode is discharging from the two edges inward, with most of the remaining capacity localized in the electrode center. We rationalize this observation as reflecting some contribution from ohmic potential losses in the electrode since electrolyte concentration and hence electrolyte overpotential are constant in the region close to the current collector as shown Fig. 4c. Ohmic loss is smallest for regions near the current collector and greatest for regions further from the current collector, causing the region near to current collector to discharge faster. For longer time, after 2000 s, the salt concentration in the region near the current collector has dropped to near zero, which caused the cell potential to decrease below 1 V and the discharge to stop, as described for high-rate discharge. The same behavior was reported by Jiang and Peng in 2016 [38]. In this article, they have shown that by increasing anode and cathode thickness by five times, a full cell suffers substantial overpotential at 1 C rate and discharge lasts only 365 s, which is far below the 1C discharge time of 3600 s. The reason to this severe capacity loss was that near-zero Li salt concentration in the electrolyte was reached at the current collector side of cathode, causing a huge overpotential which dropped the voltage to below the cut-off voltage thereby leaving a large portion of electrode capacity not accessible [38].

It is instructive to examine the electrolyte concentration and state of charge profiles for the freeze tape cast electrodes during discharge, and compare them with normal tape cast electrodes during a similar discharge. Fig. 5 a show the simulated electrolyte concentration at the middle of one cathode wall as well as in the middle of one macropore as a function of distance from the separator, at different times following the start of discharge, for a freeze tape cast electrode of thickness 454 μm. Electrolyte concentrations in the middle of the walls and in the middle of macropores overlap all through the thickness of electrode at all times which suggests that there is no substantial concentration difference between the walls and macropores. This finding reflects the fact that Li salt needs to move only 5 μm, equal to half the thickness of the cathode wall, during discharge of these electrodes. Some diminishment in electrolyte concentration in the macropores nearest the current collector and some elevation in salt concentration near the separator are evident as discharge progresses, as was also seen for normal tape cast electrodes (Fig. 4), but they never reach a level strong enough to produce salt concentrations near zero, as was observed for rapid discharge of the normal tape cast electrodes (e.g. Fig. 4e). The macropores contain enough salt to allow for full charge and discharge of the electrode without a need for significant amounts of salt to diffuse from the direction of the separator.

Fig. 5b shows the local state of charge of a freeze tape cast electrode as a function of distance from the current collector, for various times following the start of discharge. In agreement with findings for the normal tape cast electrode, discharge occurs quickly in the region near the separator, probably because of the increase in local salt concentration there as the salt is consumed throughout the electrode as discharge proceeds. At the same time, the electrode material near the current collector also discharges quickly. The reason for this is probably a combination of the ready availability of lithium salt from the macropores, which prevents strong salt depletion near the current collector, and the possible action of ohmic loss from low electronic conduction in the slabs of electrode material. Local current density within the active material slabs is higher for the freeze tape cast electrodes than for the normal tape cast electrodes because the freeze tape cast electrodes have only half as much area in contact with the current collector. The higher current density gives higher ohmic losses along the length of the electrode material slab, which are exacerbated because discharge occurs at high rates in regions near the separator. The high ohmic losses cause the electrode regions near the current collector to have the lowest overpotential, which means those regions of active material also undergo fast discharge. The Li ion concentration in the electrolyte near the current collector starts to diminish initially due to its consumption as a result of intercalation into active material. As time passes, discharge regions move toward the middle of the electrode resulting in reduction in Li ion consumption in the electrolyte near current collector. This leads to a Li ion concentration increase near the current collector which causes reduction of concentration difference throughout the electrode. The net effect is that the electrode charges from the two ends in towards the middle, with the active material regions that are centered between the separator and the current collector being the last to be discharged. These findings highlight the value of simulation in understanding how electrodes charge and discharge. Insights such as this regarding the spatial distribution of electrode discharge over time are not obtained from discharge curves. However, they are clear from simulations.

Fig. 6 presents simulation results showing areal capacity as a function of C rate for normal and freeze tape cast electrodes having variable mass loading, thicknesses and tortuosity. Solid lines are for electrodes with tortuosity of 5 while dash lines are for electrodes with tortuosity of 10. For normal tape cast electrodes having thickness of 150 and 250 μm (mass loadings of 18.1 and 30.22 mg cm^{-2}), doubling tortuosity at each thickness causes rate capability to be reduced by half. Capacity starts to fall off from its maximum at C rates of 3, and 1 in electrode with thickness of 150 and 250 μm and tortuosity of 5, while it reduces to 2 and 0.5 when tortuosity is 10. In contrast, freeze tape cast electrodes with thickness of 272.7 and 454.5 μm, with the same mass loading as normal tape cast electrode with the thickness of 150 and 250 μm, show stable maximum areal capacity up to C rates of 6 and 2, about double the maximum C rates of their normal tape cast electrode counterpart. In addition, doubling the tortuosity has no profound effect on areal capacity of freeze tape cast electrodes.

Gallagher and co-workers have presented an expression for penetration depth of electrolyte in an electrode. Their expression is given as equation (24) [39]:

$$L_d = \frac{\varepsilon}{\tau}\frac{D_l F}{\left(1 - t_+^0\right) I} \qquad \text{Eq 24}$$

In this equation, ϵ is porosity, τ is tortuosity, D_l is Li salt diffusion coefficient, t_+^0 is the lithium transference number, I is current density, and F is the Faraday constant. One can then note that the volumetric capacity (QV) is equal to the thickness of electrode (L) multiplied by areal capacity (QA). Combining this expression with equation (24), one can thus write [39]:

$$Q_A = \frac{L}{Ld}\frac{\varepsilon}{\tau}\frac{D_l F}{\left(1 - t_+^0\right) I} Q_V \qquad \text{Eq 25}$$

These expressions are useful because they allow for presentation and comparison of discharge capacity data for a wide range of conditions, as plots of the fraction of areal capacity obtained as a function of the electrode thickness normalized to the quantity L_d. Fig. 7 presents plots of this type for normal tape cast electrodes (Fig. 7a) and freeze tape cast

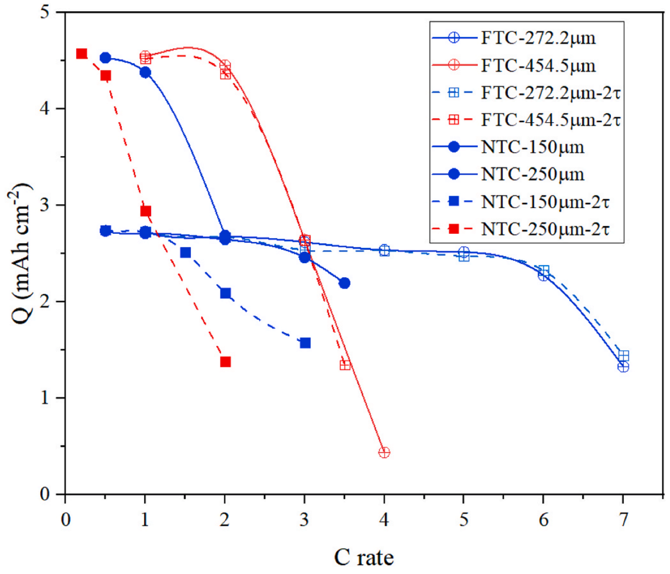

Fig. 6. Areal capacity of normal and freeze tape cast electrodes with the same mass loading as a function of discharge rate for two electrode thicknesses and tortuosities.

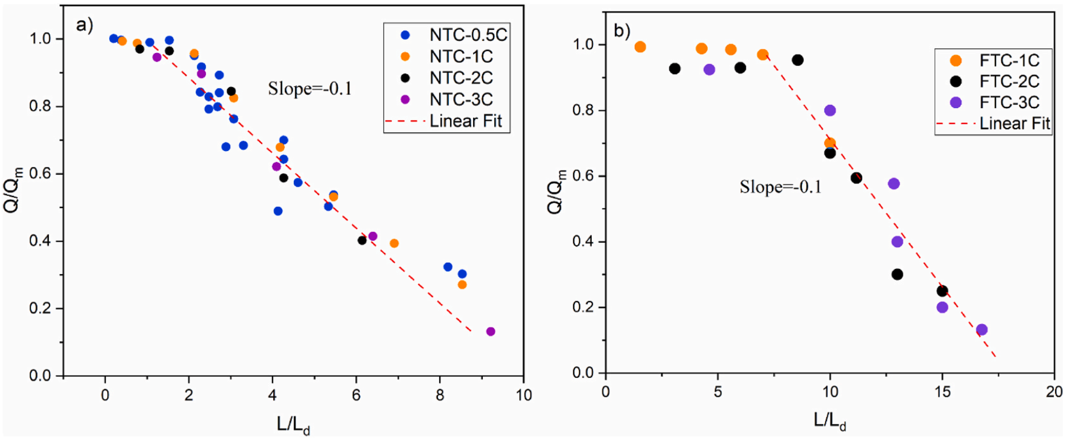

Fig. 7. Simulated results of normalized capacity for (a) normal tape cast and (b) freeze tape cast electrodes, with varying electrode thickness and discharge rate. Symbols represent normalized discharge capacity at a constant discharge time or C-rate for different electrode thicknesses that utilize a constant set of physical properties.

electrodes (Fig. 7b) of varying electrode thicknesses and at different discharge rates.

In the case of a normal tape cast electrode structure, as long as L/L_d is lower than 1.8, the capacity is near the maximum value for a given electrode (i.e., Q/Q_m is near 1.0). However, the accessible capacity begins to deviate strongly from the maximum available capacity as electrode thickness becomes more than 1.8 times the electrolyte penetration depth. Interestingly, above the cutoff L/L_d value of 1.8, all of the Q/Q$_{\text{m}}$ values with different thickness and C rates fall along a line with the slope of −0.1. For the freeze tape cast electrodes, a similar behavior is seen but the critical L/L_d increases to the value of 8, compared to 1.8 for normal tape cast electrodes. The observation reflects the fact that electrolyte accessibility is greater for electrodes having the macroporous freeze tape geometry. The slope of the line along which normalized capacity decreases as a function of L/L_d remained the same as that for normal tape cast.

Fig. 8 a, b show specific energy obtained from simulations as a function of electrode thickness (or mass loading) for normal and freeze tape cast electrodes at different C rates. Specific energy was calculated considering the weight of just the active material. As shown in Fig. 8a, discharging a normal tape cast electrode in 2 h ($C = 0.5$) is slow enough that the electrode can deliver its maximum specific energy of 225 Wh/kg even at high thickness. By increasing C discharge rate, this tolerance to electrode thickness reduces rapidly causing the drastic loss of apparent specific energy. In addition, by doubling the tortuosity from 5 to 10, specific energy fading of normal tape cast electrodes increases sharply. On the other hand, electrodes having the anisotropic porous microstructure characteristic of freeze tape casting, shown in Fig. 8b, show substantially less fading of specific energy with increasing electrode thickness, mass loading, and tortuosity, enabling it to deliver higher specific energy compared to normal tape cast electrode.

A presentation of specific energy *vs* a ratio of L/L_d can also be a useful way of comparing results for a wide range of electrode thicknesses and conditions. Fig. 8c presents specific energy for the normal and freeze tape cast electrodes with tortuosity of 5 considered in this work as a function of L/L_d. This plot shows a clear difference between normal and freeze tape cast electrodes, with specific energy always greater for freeze cast compared with normal tape cast for a given L/L_d value. Maximum specific energy values are similar for normal and freeze tape cast electrodes because in both cases the energy is normalized to mass loading. Specific energy of normal tape cast electrodes drops rapidly along a line with slope of about −25 while freeze tape cast electrodes shows a milder drop of specific energy (slope of about −14) compared to normal tape cast electrode.

4. Conclusions

A combined simulation and experiment study was performed on electrodes having isotropic and anisotropic porous microstructure. The key finding of this work from both experiment and simulation is that macropores can significantly improve the ability of thick electrodes with high mass loading to rapidly discharge. Simulation shows that for mass loadings as high as 30 mg cm^{-2}, electrodes having a macroporous microstructure created by freeze-tape casting can deliver the same areal capacity as normal tape cast electrodes but at three times faster rate. Moreover, electrochemical performance metrics such as capacity and specific energy of electrodes having a freeze tape cast microstructure are substantially improved as compared to electrodes having a normal tape cast microstructure. Performance metrics for freeze tape cast electrodes are also approximately independent of tortuosity in the active-material regions, which is not the case for electrodes prepared using normal tape cast methods.

Macropores which are obtained by freeze tape casting are elongated through the thickness of the electrode and act as reservoirs of electrolyte causing fast transport of Li salt, as a result of which electrolyte is always present near the electrode active material and is not strongly depleted during discharge. On the contrary, normal tape cast electrodes lack this macroporosity which causes the limitation of Li salt rapid transport from Li metal toward the current collector, causing a large electrolyte overpotential and voltage drop. Simulations enable an assessment of spatial and temporal variation of electrolyte concentration and electrode state of charge under different discharge rates. Knowledge of how electrolyte concentrations change over time in different locations in the electrodes, and the effect of electrode microstructure on those local electrolyte concentration variations, will help in the design of next-generation electrodes having engineered porous architecture to achieve rapid charge/discharge with high mass loading.

Declaration of competing interest

The authors declare that they have no known competing financial interests or personal relationships that could have appeared to influence the work reported in this paper.

CRediT authorship contribution statement

Milad Azami-Ghadkolai: Methodology, Software, Validation, Formal analysis, Investigation, Writing - original draft, Writing - review & editing, Visualization. **Mehrdad Yousefi:** Methodology, Software, Writing - review & editing, Visualization. **Srikanth Allu:** Validation,

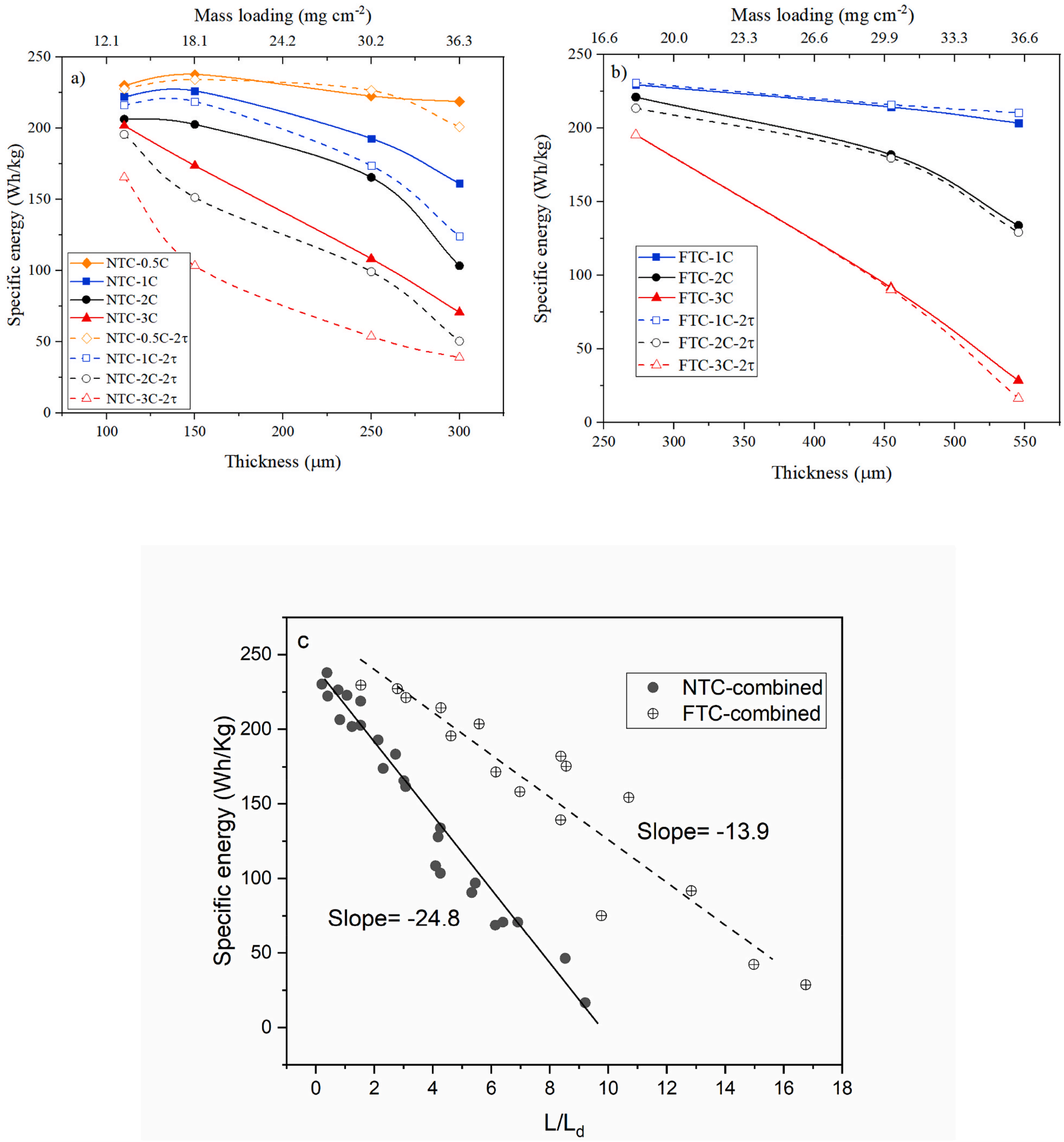

Fig. 8. *Specific energy as a function thickness, mass loading, C rate and tortuosity for a) normal b) freeze tape cast electrode. (c) Specific energy as a function normalized electrode thickness with tortuosity of 5 for normal* and *freeze tape cast electrodes. Note: specific energy calculated based on electrode alone not considering inactive components.*

Writing - review & editing. **Stephen Creager:** Conceptualization, Validation, Writing - review & editing, Supervision. **Rajendra Bordia:** Conceptualization, Methodology, Validation, Writing - review & editing, Supervision, Project administration, Funding acquisition.

Acknowledgements

This work was supported in part by the National Science Foundation EPSCoR Program under NSF Award # OIA-1655740. Any Opinions, findings and conclusions or recommendations expressed in this material are those of the author(s) and do not necessarily reflect those of the National Science Foundation. Clemson University is acknowledged for a generous allotment of computer time on the Palmetto cluster and for providing access to the COMSOL 5.3a modelling tool for this research. In addition, the authors acknowledge useful scientific discussions with Prof. Ulf Schiller from the Materials Science and Engineering Department at Clemson University.

Appendix A. Supplementary data

Supplementary data to this article can be found online at https://doi.org/10.1016/j.jpowsour.2020.228490.

References

[1] C. Fongy, A.-C. Gaillot, S. Jouanneau, D. Guyomard, B. Lestriez, J. Electrochem. Soc. 157 (2010) A885–A891.

[2] J.S. Sakamoto, B. Dunn, J. Mater. Chem. 12 (2002) 2859–2861.
[3] N.S. Ergang, J.C. Lytle, K.T. Lee, S.M. Oh, W.H. Smyrl, A. Stein, Adv. Mater. 18 (2006) 1750–1753.
[4] B. Fang, M.-S. Kim, J.H. Kim, S. Lim, J.-S. Yu, J. Mater. Chem. 20 (2010) 10253–10259.
[5] Y.G. Guo, Y.S. Hu, W. Sigle, J. Maier, Adv. Mater. 19 (2007) 2087–2091.
[6] Y.-S. Hu, P. Adelhelm, B.M. Smarsly, S. Hore, M. Antonietti, J. Maier, Adv. Funct. Mater. 17 (2007) 1873–1878.
[7] H. Zhang, X. Yu, P.V. Braun, Nat. Nanotechnol. 6 (2011) 277.
[8] M. Gaberscek, R. Dominko, M. Bele, M. Remskar, J. Jamnik, Solid State Ionics 177 (2006) 3015–3022.
[9] R. Dominko, M. Bele, J.-M. Goupil, M. Gaberscek, D. Hanzel, I. Arcon, J. Jamnik, Chem. Mater. 19 (2007) 2960–2969.
[10] A. Imhof, D. Pine, Nature 389 (1997) 948.
[11] H. Zhang, A.I. Cooper, Soft Matter 1 (2005) 107–113.
[12] C.M. Doherty, R.A. Caruso, B.M. Smarsly, C.J. Drummond, Chem. Mater. 21 (2009) 2895–2903.
[13] S.-W. Woo, K. Dokko, K. Kanamura, Electrochim. Acta 53 (2007) 79–82.
[14] S. Behr, R. Amin, Y. Chiang, A. Tomsia, Ceram. Forum Int. (2015) E39–E43.
[15] M.A. Ghadkolai, S. Creager, J. Nanda, R.K. Bordia, J. Electrochem. Soc. 164 (2017) A2603–A2610.
[16] P.S. Niksiar, F.Y. Su, M.B. Frank, T.A. Ogden, S.E. Naleway, M.A. Meyers, J. McKittrick, M.M. Porter, Ceramics 2 (2019) 208–234.
[17] P. Niksiar, M.B. Frank, J. McKittrick, M.M. Porter, J. Mater. Res. Technol. 8 (2019) 2247–2254.
[18] A. Stein, Microporous Mesoporous Mater. 44 (2001) 227–239.
[19] R. Amin, B. Delattre, A.P. Tomsia, Y.-M. Chiang, ACS Appl. Energy Mater. 1 (2018) 4976–4981.
[20] B. Delattre, R. Amin, J. Sander, J. De Coninck, A.P. Tomsia, Y.-M. Chiang, J. Electrochem. Soc. 165 (2018) A388–A395.
[21] M. Doyle, T.F. Fuller, J. Newman, J. Electrochem. Soc. 140 (1993) 1526–1533.
[22] T.F. Fuller, M. Doyle, J. Newman, J. Electrochem. Soc. 141 (1994) 1–10.
[23] M. Doyle, J. Newman, A.S. Gozdz, C.N. Schmutz, J.M. Tarascon, J. Electrochem. Soc. 143 (1996) 1890–1903.
[24] D.E. Stephenson, E.M. Hartman, J.N. Harb, D.R. Wheeler, J. Electrochem. Soc. 154 (2007) A1146–A1155.
[25] J. Landesfeind, A. Eldiven, H.A. Gasteiger, J. Electrochem. Soc. 165 (2018) A1122–A1128.
[26] G. Xu, P. Han, S. Dong, H. Liu, G. Cui, L. Chen, Coord. Chem. Rev. 343 (2017) 139–184.
[27] B. Zhao, R. Ran, M. Liu, Z. Shao, Mater. Sci. Eng. R Rep. 98 (2015) 1–71.
[28] L. Wang, Z. Zhang, G. Liang, X. Ou, Y. Xu, Powder Technol. 215 (2012) 79–84.
[29] C. Lina, Y. Xinb, F. Chengb, M.O. Lai, H. Zhoub, L. Lua.
[30] S.C. Maiti, M.A. Ghadkolai, R.K. Bordia, C. Ghoroi, Ceram. Int. 44 (2018) 12580–12592.
[31] Y. Ye, Y. Shi, N. Cai, J. Lee, X. He, J. Power Sources 199 (2012) 227–238.
[32] S. Allu, S. Kalnaus, S. Simunovic, J. Nanda, J.A. Turner, S. Pannala, J. Power Sources 325 (2016) 42–50.
[33] T. Danner, M. Singh, S. Hein, J. Kaiser, H. Hahn, A. Latz, J. Power Sources 334 (2016) 191–201.
[34] C.L. Cobb, M. Blanco, J. Power Sources 249 (2014) 357–366.
[35] A.G. Kashkooli, G. Lui, S. Farhad, D.U. Lee, K. Feng, A. Yu, Z. Chen, Electrochim. Acta 196 (2016) 33–40.
[36] A. Nyman, M. Behm, G. Lindbergh, Electrochim. Acta 53 (2008) 6356–6365.
[37] M. Rashid, A. Sahoo, A. Gupta, Y. Sharma, Electrochim. Acta 283 (2018) 313–326.
[38] F. Jiang, P. Peng, Sci. Rep. 6 (2016) 32639.
[39] K.G. Gallagher, S.E. Trask, C. Bauer, T. Woehrle, S.F. Lux, M. Tschech, P. Lamp, B. J. Polzin, S. Ha, B. Long, Q. Wu, W. Lu, D.W. Dees, A.N. Jansen, J. Electrochem. Soc. 163 (2016) A138–A149.